EXTENDED PDF FORMAT
SPONSORED BY

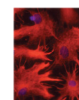

Travel Grants Available
Neuroscience 2014
Application Deadline: July 31st
>Apply Now
www.rndsystems.com

The valley Hall effect in MoS_2 transistors

K. F. Mak *et al.*

Science **344**, 1489 (2014);
DOI: 10.1126/science.1250140

This copy is for your personal, non-commercial use only.

If you wish to distribute this article to others, you can order high-quality copies for your colleagues, clients, or customers by clicking here.

Permission to republish or repurpose articles or portions of articles can be obtained by following the guidelines here.

The following resources related to this article are available online at www.sciencemag.org (this information is current as of July 28, 2014):

Updated information and services, including high-resolution figures, can be found in the online version of this article at:
http://www.sciencemag.org/content/344/6191/1489.full.html

Supporting Online Material can be found at:
http://www.sciencemag.org/content/suppl/2014/06/25/344.6191.1489.DC1.html

This article **cites 33 articles**, 4 of which can be accessed free:
http://www.sciencemag.org/content/344/6191/1489.full.html#ref-list-1

This article appears in the following **subject collections:**
Physics
http://www.sciencemag.org/cgi/collection/physics

Downloaded from www.sciencemag.org on July 28, 2014

Science (print ISSN 0036-8075; online ISSN 1095-9203) is published weekly, except the last week in December, by the American Association for the Advancement of Science, 1200 New York Avenue NW, Washington, DC 20005. Copyright 2014 by the American Association for the Advancement of Science; all rights reserved. The title *Science* is a registered trademark of AAAS.

REFERENCES AND NOTES

1. V. B. Braginskiĭ, Y. I. Vorontsov, *Sov. Phys. Usp.* **17**, 644 (1975).
2. C. M. Caves, *Phys. Rev. Lett.* **45**, 75–79 (1980).
3. C. M. Caves, K. S. Thorne, R. W. P. Drever, V. D. Sandberg, M. Zimmermann, *Rev. Mod. Phys.* **52**, 341–392 (1980).
4. K. S. Thorne, *Rev. Mod. Phys.* **52**, 285–297 (1980).
5. P. F. Cohadon, A. Heidmann, M. Pinard, *Phys. Rev. Lett.* **83**, 3174–3177 (1999).
6. I. Tittonen *et al.*, *Phys. Rev. A* **59**, 1038–1044 (1999).
7. K. W. Murch, K. L. Moore, S. Gupta, D. M. Stamper-Kurn, *Nat. Phys.* **4**, 561–564 (2008).
8. T. P. Purdy, R. W. Peterson, C. A. Regal, *Science* **339**, 801–804 (2013).
9. D. Rugar, R. Budakian, H. J. Mamin, B. W. Chui, *Nature* **430**, 329–332 (2004).
10. J. M. Nichol, E. R. Hemesath, L. J. Lauhon, R. Budakian, *Appl. Phys. Lett.* **93**, 193110 (2008).
11. B. Abbott *et al.*, *New J. Phys.* **11**, 073032 (2009).
12. J. Moser *et al.*, *Nat. Nanotechnol.* **8**, 493–496 (2013).
13. M. J. Biercuk, H. Uys, J. W. Britton, A. P. VanDevender, J. J. Bollinger, *Nat. Nanotechnol.* **5**, 646–650 (2010).
14. G. Anetsberger *et al.*, *Phys. Rev. A* **82**, 061804 (2010).
15. T. Westphal *et al.*, *Phys. Rev. A* **85**, 063806 (2012).
16. F. Marquardt, S. M. Girvin, *Physics* **2**, 40 (2009).
17. G. Anetsberger *et al.*, *Nat. Phys.* **5**, 909–914 (2009).
18. J. D. Teufel, T. Donner, M. A. Castellanos-Beltran, J. W. Harlow, K. W. Lehnert, *Nat. Nanotechnol.* **4**, 820–823 (2009).
19. S. Gupta, K. L. Moore, K. W. Murch, D. M. Stamper-Kurn, *Phys. Rev. Lett.* **99**, 213601 (2007).
20. F. Brennecke, S. Ritter, T. Donner, T. Esslinger, *Science* **322**, 235–238 (2008).
21. T. P. Purdy *et al.*, *Phys. Rev. Lett.* **105**, 133602 (2010).
22. Materials and methods are available as supporting materials on *Science* Online.
23. T. Botter, D. W. C. Brooks, S. Schreppler, N. Brahms, D. M. Stamper-Kurn, *Phys. Rev. Lett.* **110**, 153001 (2013).
24. F. Marsili *et al.*, *Nat. Photonics* **7**, 210–214 (2013).
25. A. A. Clerk, M. H. Devoret, S. M. Girvin, F. Marquardt, R. J. Schoelkopf, *Rev. Mod. Phys.* **82**, 1155–1208 (2010).
26. M. Aspelmeyer, T. J. Kippenberg, F. Marquardt, "Cavity optomechanics" (2013); http://arxiv.org/abs/1303.0733.
27. T. Caniard, P. Verlot, T. Briant, P.-F. Cohadon, A. Heidmann, *Phys. Rev. Lett.* **99**, 110801 (2007).
28. J. B. Hertzberg *et al.*, *Nat. Phys.* **6**, 213–217 (2009).
29. M. Tsang, C. M. Caves, *Phys. Rev. Lett.* **105**, 123601 (2010).
30. X. Xu, J. M. Taylor, "Beating the standard quantum limit for force sensing with a coupled two-mode optomechanical system" (2013); http://arxiv.org/abs/1303.7469.
31. M. J. Woolley, A. A. Clerk, *Phys. Rev. A* **87**, 063846 (2013).
32. V. Braginsky, F. Khalili, K. Thorne, *Quantum Measurement* (Cambridge Univ. Press, Cambridge, 1995).
33. A. A. Geraci, S. B. Papp, J. Kitching, *Phys. Rev. Lett.* **105**, 101101 (2010).

ACKNOWLEDGMENTS

This work was supported by the Air Force Office of Scientific Research and NSF. S.S. was supported by the U.S. Department of Defense through the National Defense Science and Engineering Graduate Fellowship program.

SUPPLEMENTARY MATERIALS

www.sciencemag.org/content/344/6191/1486/suppl/DC1
Materials and Methods
Figs. S1 and S2
References (*34–36*)

17 December 2013; accepted 19 May 2014
10.1126/science.1249850

VALLEYTRONICS

The valley Hall effect in MoS_2 transistors

K. F. Mak,[1,2]* K. L. McGill,[2] J. Park,[1,3] P. L. McEuen[1,2]*

Electrons in two-dimensional crystals with a honeycomb lattice structure possess a valley degree of freedom (DOF) in addition to charge and spin. These systems are predicted to exhibit an anomalous Hall effect whose sign depends on the valley index. Here, we report the observation of this so-called valley Hall effect (VHE). Monolayer MoS_2 transistors are illuminated with circularly polarized light, which preferentially excites electrons into a specific valley, causing a finite anomalous Hall voltage whose sign is controlled by the helicity of the light. No anomalous Hall effect is observed in bilayer devices, which have crystal inversion symmetry. Our observation of the VHE opens up new possibilities for using the valley DOF as an information carrier in next-generation electronics and optoelectronics.

The charge and spin degrees of freedom (DOF) of electrons are at the heart of modern electronics. They form the basis for a wide range of applications, such as transistors, photodetectors, and magnetic memory devices. Electrons in two-dimensional (2D) crystals that have a honeycomb lattice structure possess an extra valley DOF (*1*) in addition to charge and spin. This new DOF has the potential to be used as an information carrier in next-generation electronics (*2–6*) and optoelectronics (*7*). Valley-dependent electronics and optoelectronics based on semimetallic graphene, a representative 2D crystal, have been theoretically proposed (*2–5*), but the presence of inversion symmetry in the crystal structure of pristine graphene makes both optical and electrical control of the valley DOF difficult.

In contrast, monolayer molybdenum disulfide (MoS_2), a 2D direct band gap semiconductor (*8*, *9*) that possesses a staggered honeycomb lattice structure, is inversion asymmetric. Its fundamental direct energy gaps are located at the K and K′ valleys of the Brillouin zone (Fig. 1A). Because of the broken inversion symmetry in its crystal structure, electrons in the two valleys experience effective magnetic fields [proportional to the Berry curvature, $\vec{\Omega}$ (*4*)] with equal magnitudes but opposite signs (Fig. 1A). Such a magnetic field not only defines the optical selection rules (*6*) that allow optical pumping of valley-polarized carriers by circularly polarized photons (*10–14*), it also generates an anomalous velocity for the charge carriers (*6*, *15*). Namely, when the semiconductor channel is biased, electrons from different valleys experience opposite Lorentz-like forces and so move in opposite directions perpendicular to the drift current, which is a phenomenon called the valley Hall effect (VHE) (*4–6*, *16*). The VHE originates from the coupling of the valley DOF to the orbital motion of the electrons (*4*, *10*). This is closely analogous to the spin Hall effect (SHE) (*17–21*) with the spin-polarized electrons replaced by valley-polarized carriers.

Under time-reversal symmetry, equal amounts of Hall current from each valley flow in opposite directions so that no net Hall voltage is produced. To measure the valley Hall effect, we explicitly break time-reversal symmetry by shining circularly polarized light onto a Hall bar device (Fig. 1B). A population imbalance between the two valleys (a valley polarization) is thus created. Under a finite bias, both photoconduction (associated with the normal drift current of the photoexcited charge carriers) and a net transverse Hall voltage (associated with the VHE) should occur (*5*, *6*). The presence of a photoinduced anomalous Hall effect (AHE) driven by a net valley polarization is the experimental manifestation of the VHE in monolayer MoS_2.

The magnitude of the AHE is determined by an anomalous Hall conductivity σ_H. Including both the intrinsic Berry curvature effect and the extrinsic side-jump scattering contribution (*22*), (*4*) predicts the following expression for σ_H

$$\sigma_H \approx -\frac{\hbar^2 \pi \Delta n_v}{2 m_e E_g} \frac{e^2}{h} \quad (1)$$

[A derivation is provided in (*23*), section 2.1]. The anomalous Hall conductivity σ_H is linear in $n_v \equiv n_K - n_{K'}$, the photoexcited carrier density imbalance between the K (n_K) and K′ ($n_{K'}$) valleys, and is dependent only on the intrinsic band parameters under the assumption of no intervalley scattering (*4*, *24*). Here, e is elementary charge, h is Planck's constant, is h divided by 2π, $m_e \approx 0.4 m_0$ is the electron band mass (m_0 is the free electron mass) (*25*), and $E_g \approx 1.9$ eV is the band gap of monolayer MoS_2 (*8*). Equation 1 thus allows for a quantitative comparison between experiment and theory. We only need to consider the density of the majority carriers, which are electrons in our devices.

An optical image of one of the MoS_2 Hall bar devices (labeled as M1) that we have investigated

[1]Kavli Institute at Cornell for Nanoscale Science, Ithaca, NY 14853, USA. [2]Laboratory of Atomic and Solid State Physics, Cornell University, Ithaca, NY 14853, USA. [3]Department of Chemistry and Chemical Biology, Cornell University, Ithaca, NY 14853, USA.
*Corresponding author. E-mail: plm23@cornell.edu (P.L.M.); km627@cornell.edu (K.F.M.)

in this study is shown in Fig. 1. A bias voltage (V_x) is applied along the short channel, and the longitudinal current (I_x) is measured. The Hall voltage (V_H, the voltage difference between contacts A and B) is simultaneously measured, and a back gate voltage (V_g) is applied to the silicon substrate in order to continuously vary the channel doping level. The V_g-dependence of the conductivity of device M1 (σ_{xx}) extracted from two- and four-point measurements is shown in Fig. 1C. Unless otherwise indicated, all measurements were performed on monolayer MoS_2 at 77 K (experimental details are provided in (*23*), sections 1.1 and 1.2). The usual n-type field effect transistor behavior is seen (*26*). We also see that the two-point (measured at V_x = 0.5 V under the geometry shown in Fig. 1B) and four-point [measured by swapping the drain and the B contacts in Fig. 1B, and taking into account a geometric factor of ln2/π (*27*)] conductivities are similar in magnitude, indicating near-ohmic contacts in our device (*28*). Although the I_x-V_x characteristic shows the presence of Schottky barriers at small bias (Fig. 1C, inset), it has little influence on our measurements at high bias. A four-point carrier mobility of 98 $cm^2 V^{-1} s^{-1}$ and two-point carrier mobility of 61 $cm^2 V^{-1} s^{-1}$ are extracted at high V_g, where the σ_{xx}-V_g dependence becomes linear [(*23*), section 2.2].

In Fig. 1D, we examine the photoresponse of our device; this allows us to identify the appropriate photon energy (E) for efficient injection of valley-polarized carriers (*11*, *29*). Shown in the inset is the photocurrent ΔI_x as a function of V_x (at V_g = 0 V) under different laser excitation intensities P; the data were taken with a focused laser beam (centered at 1.9 eV) located at the center of the device. Similar to the effect of electrical gating (Fig. 1C, inset), the effect of incident photons is to increase the channel conductivity σ_{xx}, which indicates that photoconduction is the main mechanism driving the photoresponse in our device (*30*); photocurrent generation under zero bias is negligible [(*23*), section 2.3]. The change in conductivity with and without laser illumination $\Delta\sigma_{xx} \equiv \sigma_{xx,\text{light}} - \sigma_{xx,\text{dark}}$ as a function of incident photon energies E (Fig. 1D) clearly shows the A (at $E \approx$ 1.9 eV) and B (at $E \approx$ 2.1 eV) resonances of monolayer MoS_2 (*8*).

By parking the laser spot at the center of the device, we studied the Hall response under on-resonance excitation (centered at $E \approx$ 1.9 eV). To enhance our detection sensitivity, we modulated the polarization state of the incident light at 50 kHz by use of a photoelastic modulator and measured the anomalous Hall voltage V_H with a lock-in amplifier [(*23*), section 1.2]. Under quarter-wave modulation ($\Delta\lambda$ = 1/4), the degree of excitation ellipticity can be continuously varied by changing θ, the angle of incidence of the linearly polarized light with respect to the fast axis of the modulator. On the other hand, half-wave modulation ($\Delta\lambda$ = 1/2) allows us to modulate linear excitations between –θ and θ at 100 kHz, which is twice the fundamental frequency. To indicate the special case of quarter-wave modulation with θ = 45°, in which the polarization is modulated from right- to left- handed, or θ =–45°, in which the polarization is modulated from left- to right-handed, we use the notations R-L and L-R below, respectively. All of the observations made below have been repeated on multiple devices [six devices for monolayers and two devices for bilayers (figs. S3 to S8 and S10)].

In Fig. 2A, we show the V_x-dependence of the anomalous Hall voltage (V_H) at V_g = 0 V [(*23*), sections 2.4 to 2.6]. A small but finite V_H that scales linearly with V_x is observed under R-L modulation (Fig. 2A, solid red line). This is the signature of a photoinduced AHE driven by a net valley polarization. Given the geometry of electrical connections shown in Fig. 1B, a positive Hall voltage under R-L modulation for a positive bias is observed. It is consistent with the prediction of a side-jump–dominated VHE (Eq. 1) (*4*, *6*). The sign of the signal is reversed when the excitation is changed to L-R modulation (dashed red line). In contrast, no net Hall voltage is seen when we switch to a linear (s-p) modulation (Fig. 2A, dotted red line) [measurements on other monolayer devices are provided in fig. S4].

To study the polarization dependence carefully, the anomalous Hall resistance $R_H = V_H/I_x$ as a function of the angle θ is shown in Fig. 2B for both the quarter- and half-wave modulations. We see that the Hall resistance R_H exhibits a sine dependence on θ under quarter-wave modulation. A maximum Hall resistance of ~2 ohms is measured under an excitation intensity of ~150 μW μm^{-2}. For comparison, zero Hall resistance is observed under half-wave modulation. Our results are consistent with recent experimental observations of a net valley polarization under the optical excitation of the A resonance with circularly polarized light (*10*–*14*). The sine dependence of

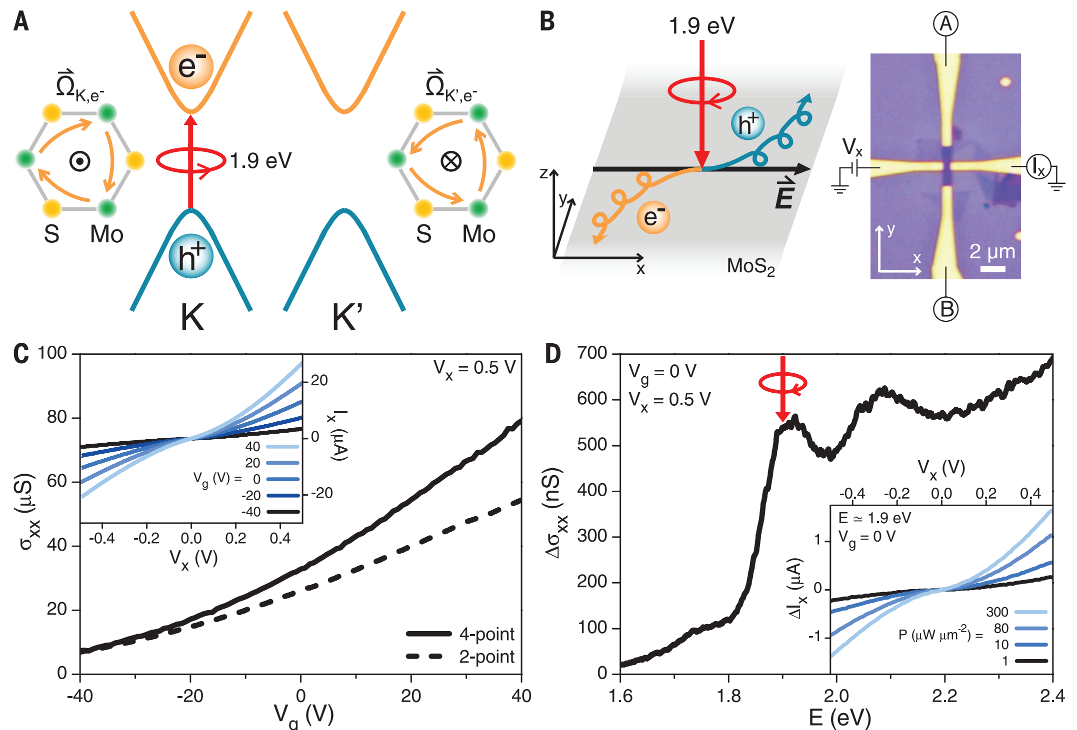

Fig. 1. Monolayer MoS_2 Hall bar device. (**A**) Schematics of the valley-dependent optical selection rules and the electrons at the K and K′ valleys that possess opposite Berry curvatures $\vec{\Omega}$. The orange arrows represent the clockwise and counterclockwise hopping motions of the K and K′ electrons. (**B**) Schematic of a photoinduced AHE driven by a net valley polarization (left) and an image of the Hall bar device (right). In the schematic, the intrinsic plus side-jump contribution as predicted by Eq. 1 is shown. (**C**) Two-point (dashed line, V_x = 0.5 V) and four-point (solid line) conductivities of the device as a function of back gate voltage V_g. (Inset) Source-drain bias (V_x) dependence of the current along the longitudinal (I_x) at different back gate voltages V_g. (**D**) The change in conductivity $\Delta\sigma_{xx}$ as a function of incident photon energy E under laser illumination. The arrow indicates the excitation energy used in most of the measurements in this paper, $E \approx$ 1.9 eV. (Inset) Source-drain bias (V_x) dependence of the photocurrent (ΔI_x) at different incident laser intensities P (V_g = 0 V).

the quarter-wave modulation data reveals the linear relationship between the degree of valley polarization and the excitation ellipticity (5, 6). Specifically, no net valley polarization is generated under linearly polarized excitations.

The possible existence of the photoinduced AHE in bilayer MoS_2 devices is investigated under on-resonance excitation and is shown in Fig. 2A [electrical characterization of our bilayer device is provided in (23), section 2.7]. No noticeable Hall voltage (more than a factor of 10 smaller than the monolayer) under R-L modulation (as well as under L-R) is observed (Fig. 2A, solid blue line). The absence of the AHE is further illustrated in Fig. 2B. The Hall resistance in the bilayer device is nearly zero for all θ (Fig. 2B, solid blue dots). The stark contrast between mono- and bilayer devices therefore suggests that an intervalley population imbalance is required to drive the AHE. No such imbalance can be produced in bilayer MoS_2 (4–6) because the inversion symmetry is restored in its crystal structure (11, 14, 31).

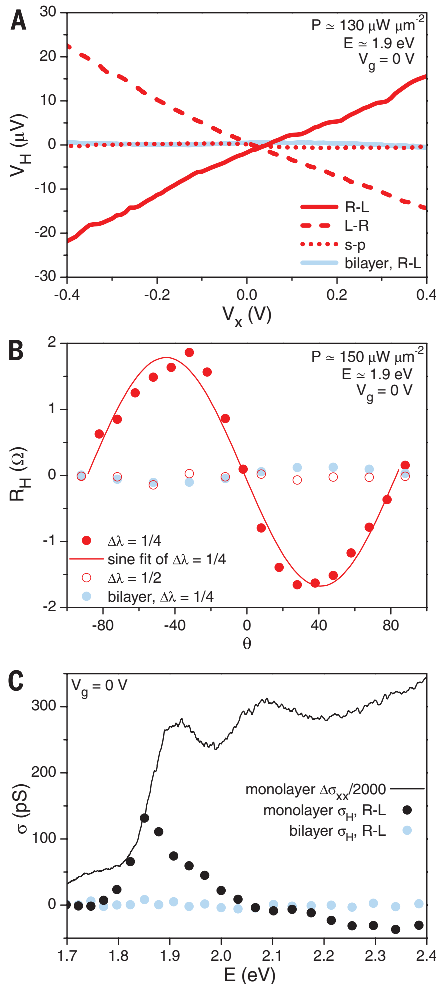

Fig. 2. The valley Hall effect. (**A**) The source-drain bias (V_x) dependence of the Hall voltage (V_H) for the monolayer device under R-L (red solid line), L-R (red dashed line), and half-wave s-p modulations (red dotted line). Results from the bilayer device under R-L modulation (blue solid line) are also shown. (**B**) The anomalous Hall resistance of the monolayer device as a function of the incidence angle θ under quarter-wave (Δλ = 1/4, solid red circles) and half-wave (Δλ = 1/2, open red circles) modulations. Results for the bilayer device under quarter-wave modulation are also shown (blue circles). (**C**) Energy dependence of the change in conductivity $\Delta\sigma_{xx}$ (black curve) and of the anomalous Hall conductivity σ_H (black and blue circles for the mono- and bilayer devices, respectively). The latter is obtained under R-L modulation.

Last, the effect of the intervalley relaxation of excited carriers on the AHE in MoS_2 monolayers is depicted in Fig. 2C. The dependences of the anomalous Hall conductivity $\sigma_H = \frac{\sigma_{xx} V_H}{V_x} \approx R_H \sigma_{xx}^2$ and of the change in conductivity $\Delta\sigma_{xx}$ on the incident photon energy E are shown. Whereas $\Delta\sigma_{xx}$ remains large and keeps increasing with increased photon energy beyond the A and B resonances (thanks to an enhancement in optical absorption), the anomalous Hall conductivity σ_H peaks near the A feature and decreases quickly to almost zero at higher photon energies. Our observation is consistent with recent optical results that indicate poor injection of valley polarization under off-resonance excitation because of the rapid intervalley relaxation of high-energy excited carriers (11, 29). For comparison, no detectable Hall conductivity is observed in the bilayer device (Fig. 2C, blue dots).

Our experimental observation of a finite AHE only in monolayer MoS_2 under on-resonance, circularly polarized excitation strongly supports our interpretation of the signal as originating from the VHE. Whereas a net spin polarization could also give rise to a finite AHE, the effect observed in our monolayer MoS_2 devices is mainly driven by a net valley polarization for the following two reasons. First, the majority of carriers responsible for photoconduction are electrons; their spin-polarized current contribution to the AHE is negligible thanks to fast spin relaxation in the nearly spin-degenerate conduction band (11, 32). Second, the coupling constant in the Hamiltonian responsible for the VHE (6) $\lambda_{VH} \sim a^2$ is much larger than that for the SHE (33) $\lambda_{SH} \sim \frac{\Delta_{SO}}{E_g} a^2 \sim 0.1a^2$, where a = 3.2 Å and Δ_{SO} = 0.16 eV are the lattice constant and the spin-orbit splitting in monolayer MoS_2 (6), respectively.

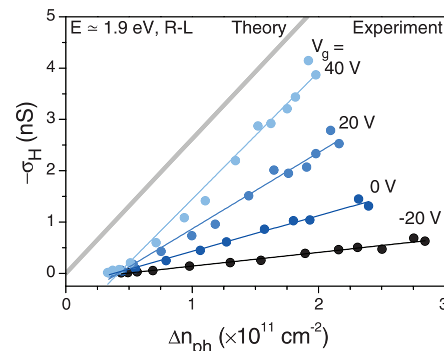

Fig. 3. Doping dependence of the anomalous Hall conductivity. The anomalous Hall conductivity σ_H under R-L modulation as a function of the charge carrier density Δn_{ph} at different gate voltages V_g. Linear fits to the experimental data are also shown. The theoretical prediction in Eq. 1 for $\Delta n_v = \Delta n_{ph}$ is shown in gray.

In order to compare our results with the theoretical prediction in Eq. 1, we studied the laser intensity (P) dependence of the photoinduced AHE under 1.9 eV excitation. For this, we first measured the gate dependence of $\Delta\sigma_{xx}$ at different incident laser powers [(23), section 2.9]. The effective change in the photoexcited carrier density Δn_{ph} can then be estimated from the relation $\Delta\sigma_{xx} = \Delta n_{ph} e\mu$, where $\mu = \frac{1}{C_g}\frac{d\sigma_{xx}}{dV_g}$ is extracted from the dark electrical measurements (Fig. 1C) with $C_g = 1.2 \times 10^{-8}$ F cm^{-2} as the back gate capacitance of our device (Δn_{ph} is very difficult to measure with conventional Hall effect methods because of a large background electron density and finite longitudinal-transverse coupling in our devices). The quantity Δn_{ph} should be equal to Δn_v if the change in conductivity $\Delta\sigma_{xx}$ is solely driven by the valley-polarized carriers that are directly excited by resonant, circularly polarized light. In reality, however, Δn_{ph} may include contributions from both valley-polarized and -unpolarized carriers; therefore, Δn_{ph} provides an upper bound for Δn_v. The anomalous Hall conductivities under R-L modulation for different gate voltages V_g are shown as functions of Δn_{ph} in Fig. 3. We also show the theoretical result predicted by Eq. 1 in the limit $\Delta n_{ph} = \Delta n_v$ in the same figure. For all gate voltages, σ_H increases linearly with Δn_{ph}, which is consistent with the theoretical prediction. The anomalous Hall conductivity σ_H also has the right order of magnitude and approaches the theoretical value at high V_g. However, the delayed onset in Fig. 3 is not understood. It may result from inaccuracy in determining the absolute photodoping density or the role of trapped charges.

In the simplest case of $\Delta n_{ph} = \Delta n_v$, the effect should be independent of V_g, which is different from our experimental observations. One possible explanation of the discrepancy is the presence of photoconduction mechanisms that do not contribute to the AHE. Such mechanisms include the relaxation of valley polarization in a portion of the photoexcited carriers and the trapping of minority carriers, which is an effect equivalent to electrostatic doping. Because the strength of disorder decreases when the device becomes more metallic at higher n-doping (ρ_{xx} versus V_g at different temperatures is provided in fig. S1), a higher portion of photoexcited carriers could maintain the valley polarization and contribute to the Hall effect. However, the slope of the σ_H versus Δn_{ph} curves keeps increasing with higher V_g and may go beyond the theoretical prediction. Unfortunately, the range of V_g applied in our experiment is limited by the breakdown of the back gate, so we were unable to explore this regime. A second possibility is a finite contribution from skew-scattering processes (22, 29) to the VHE, which has been neglected in Eq. 1. The relative importance of each of the

intrinsic and extrinsic contributions depends on the sample quality (such as the doping density and the amount of disorder). Studies of the dependence on temperature and on disorder are therefore required to better understand the doping density dependence of the VHE. Furthermore, a more accurate determination of σ_H that takes into account the fringe fields in our Hall bar device may be needed for a better quantitative comparison.

REFERENCES AND NOTES

1. A. H. Castro Neto, F. Guinea, N. M. R. Peres, K. S. Novoselov, A. K. Geim, *Rev. Mod. Phys.* **81**, 109–162 (2009).
2. A. Rycerz, J. Tworzydlo, C. W. J. Beenakker, *Nat. Phys.* **3**, 172–175 (2007).
3. A. R. Akhmerov, C. W. J. Beenakker, *Phys. Rev. Lett.* **98**, 157003 (2007).
4. D. Xiao, W. Yao, Q. Niu, *Phys. Rev. Lett.* **99**, 236809 (2007).
5. W. Yao, D. Xiao, Q. Niu, *Phys. Rev. B* **77**, 235406 (2008).
6. D. Xiao, G.-B. Liu, W. Feng, X. Xu, W. Yao, *Phys. Rev. Lett.* **108**, 196802 (2012).
7. Y. J. Zhang, T. Oka, R. Suzuki, J. T. Ye, Y. Iwasa, *Science* **344**, 725–728 (2014).
8. K. F. Mak, C. Lee, J. Hone, J. Shan, T. F. Heinz, *Phys. Rev. Lett.* **105**, 136805 (2010).
9. A. Splendiani *et al*., *Nano Lett.* **10**, 1271–1275 (2010).
10. T. Cao *et al*., *Nat. Commun.* **3**, 887 (2012).
11. K. F. Mak, K. He, J. Shan, T. F. Heinz, *Nat. Nanotechnol.* **7**, 494–498 (2012).
12. G. Sallen *et al*., *Phys. Rev. B* **86**, 081301 (2012).
13. S. Wu *et al*., *Nat. Phys.* **9**, 149–153 (2013).
14. H. Zeng, J. Dai, W. Yao, D. Xiao, X. Cui, *Nat. Nanotechnol.* **7**, 490–493 (2012).
15. D. Xiao, M.-C. Chang, Q. Niu, *Rev. Mod. Phys.* **82**, 1959–2007 (2010).
16. X. Li, F. Zhang, Q. Niu, *Phys. Rev. Lett.* **110**, 066803 (2013).
17. S. Murakami, N. Nagaosa, S.-C. Zhang, *Science* **301**, 1348–1351 (2003).
18. J. Sinova *et al*., *Phys. Rev. Lett.* **92**, 126603 (2004).
19. Y. K. Kato, R. C. Myers, A. C. Gossard, D. D. Awschalom, *Science* **306**, 1910–1913 (2004).
20. J. Wunderlich, B. Kaestner, J. Sinova, T. Jungwirth, *Phys. Rev. Lett.* **94**, 047204 (2005).
21. J. Wunderlich *et al*., *Science* **330**, 1801–1804 (2010).
22. N. Nagaosa, J. Sinova, S. Onoda, A. H. MacDonald, N. P. Ong, *Rev. Mod. Phys.* **82**, 1539–1592 (2010).
23. Materials and methods are available as supplementary materials on *Science* Online.
24. The skew scattering contribution, which is important only for high-mobility devices (*22*), is neglected in MoS_2 devices with relatively low mobility.
25. T. Cheiwchanchamnangij, W. R. L. Lambrecht, *Phys. Rev. B* **85**, 205302 (2012).
26. B. Radisavljevic, A. Radenovic, J. Brivio, V. Giacometti, A. Kis, *Nat. Nanotechnol.* **6**, 147–150 (2011).
27. L. J. van der Pauw, *Philips Techn. Rev.* **20**, 220–224 (1958).
28. B. W. H. Baugher, H. O. H. Churchill, Y. Yang, P. Jarillo-Herrero, *Nano Lett.* **13**, 4212–4216 (2013).
29. G. Kioseoglou *et al*., *Appl. Phys. Lett.* **101**, 221907 (2012).
30. O. Lopez-Sanchez, D. Lembke, M. Kayci, A. Radenovic, A. Kis, *Nat. Nanotechnol.* **8**, 497–501 (2013).
31. Strictly speaking, a bilayer device with slightly broken inversion symmetry by the substrate and/or by unintentional doping could also produce a finite VHE, but these effects are expected to be much smaller as compared with the VHE in monolayer devices (*13*).
32. Here, our assumption that only the photoexcited electrons contribute to the Hall response is reasonable because the holes are much more vulnerable to traps than are the electrons, given our highly n-doped device. Unlike the electron side, the VHE and the SHE become equivalent on the hole side owing to the spin-valley coupled valence band.
33. H.-A. Engel, B. I. Halperin, E. I. Rashba, *Phys. Rev. Lett.* **95**, 166605 (2005).

ACKNOWLEDGMENTS

We thank D. C. Ralph for his insightful suggestions and J. W. Kevek for technical support. We also thank J. Shan for many fruitful discussions and Y. You for private communications regarding the optical data on monolayer MoS_2. This research was supported by the Kavli Institute at Cornell for Nanoscale Science and the Cornell Center for Materials Research [National Science Foundation (NSF) DMR-1120296]. Additional funding was provided by the Air Force Office of Scientific Research (FA9550-10-1-0410) and the Nano-Material Technology Development Program through the National Research Foundation of Korea funded by the Ministry of Science, ICT and Future Planning (2012M3A7B4049887). Device fabrication was performed at the Cornell NanoScale Science and Technology Facility, a member of the National Nanotechnology Infrastructure Network, which is supported by NSF (grant ECCS-0335765). K.L.M. acknowledges support from the NSF Integrative Graduate Education and Research Traineeship program (DGE-0654193) and the NSF Graduate Research Fellowship Program (DGE-1144153).

SUPPLEMENTARY MATERIALS

www.sciencemag.org/content/344/6191/1489/suppl/DC1
Materials and Methods
Supplementary Text
Figs. S1 to S10
References (*34–37*)

24 December 2013; accepted 23 May 2014
10.1126/science.1250140

MACHINE LEARNING

Clustering by fast search and find of density peaks

Alex Rodriguez and Alessandro Laio

Cluster analysis is aimed at classifying elements into categories on the basis of their similarity. Its applications range from astronomy to bioinformatics, bibliometrics, and pattern recognition. We propose an approach based on the idea that cluster centers are characterized by a higher density than their neighbors and by a relatively large distance from points with higher densities. This idea forms the basis of a clustering procedure in which the number of clusters arises intuitively, outliers are automatically spotted and excluded from the analysis, and clusters are recognized regardless of their shape and of the dimensionality of the space in which they are embedded. We demonstrate the power of the algorithm on several test cases.

Clustering algorithms attempt to classify elements into categories, or clusters, on the basis of their similarity. Several different clustering strategies have been proposed (*1*), but no consensus has been reached even on the definition of a cluster. In K-means (*2*) and K-medoids (*3*) methods, clusters are groups of data characterized by a small distance to the cluster center. An objective function, typically the sum of the distance to a set of putative cluster centers, is optimized (*3–6*) until the best cluster centers candidates are found. However, because a data point is always assigned to the nearest center, these approaches are not able to detect nonspherical clusters (*7*). In distribution-based algorithms, one attempts to reproduce the observed realization of data points as a mix of predefined probability distribution functions (*8*); the accuracy of such methods depends on the capability of the trial probability to represent the data.

Clusters with an arbitrary shape are easily detected by approaches based on the local density of data points. In density-based spatial clustering of applications with noise (DBSCAN) (*9*), one chooses a density threshold, discards as noise the points in regions with densities lower than this threshold, and assigns to different clusters disconnected regions of high density. However, choosing an appropriate threshold can be nontrivial, a drawback not present in the mean-shift clustering method (*10*, *11*). There a cluster is defined as a set of points that converge to the same local maximum of the density distribution function. This method allows the finding of nonspherical clusters but works only for data defined by a set of coordinates and is computationally costly.

Here, we propose an alternative approach. Similar to the K-medoids method, it has its basis only in the distance between data points. Like DBSCAN and the mean-shift method, it is able to detect nonspherical clusters and to automatically find the correct number of clusters. The cluster centers are defined, as in the mean-shift method, as local maxima in the density of data points. However, unlike the mean-shift method, our procedure does not require embedding the data in a vector space and maximizing explicitly the density field for each data point.

The algorithm has its basis in the assumptions that cluster centers are surrounded by neighbors with lower local density and that they are at a relatively large distance from any points with a higher local density. For each data point i, we compute two quantities: its local density ρ_i and its distance δ_i from points of higher density. Both these quantities depend only on the distances d_{ij} between data points, which are assumed to satisfy the triangular inequality. The local density ρ_i of data point i is defined as

$$\rho_i = \sum_j \chi(d_{ij} - d_c) \quad (1)$$

where $\chi(x) = 1$ if $x < 0$ and $\chi(x) = 0$ otherwise, and d_c is a cutoff distance. Basically, ρ_i is equal to the number of points that are closer than d_c to point i. The algorithm is sensitive only to the relative magnitude of ρ_i in different points, implying that, for large data sets, the results of the analysis are robust with respect to the choice of d_c.

SISSA (Scuola Internazionale Superiore di Studi Avanzati), via Bonomea 265, I-34136 Trieste, Italy.
E-mail: laio@sissa.it (A.L.); alexrod@sissa.it (A.R.)